Cytometry
PART A
Journal of the International Society for Advancement of Cytometry

Automated REcognition of Tissue-associated Erythrocytes (*ARETE*)—a New Tool in Tissue Cytometry

Andreas Heindl,[1,2] Alexander K. Seewald,[2*] Theresia Thalhammer,[1] Giovanna Bises,[1] Martin Schepelmann,[1,3] Hana Uhrova,[1] Sabine Dekan,[4] Ildiko Mesteri,[4] Radu Rogojanu,[5] Isabella Ellinger[1]

[1]Department of Pathophysiology and Allergy Research, Medical University Vienna, Vienna, Austria

[2]Seewald Solutions, Vienna, Austria

[3]Cardiff School of Biosciences, Cardiff University, Cardiff, Wales, United Kingdom

[4]Clinical Department of Pathology, Medical University Vienna, Vienna, Austria

[5]TissueGnostics GmbH, Vienna, Austria

Received 10 August 2012; Revision Received 26 November 2012; Accepted 23 December 2012.

Grant sponsor: FFG/Austria (Bridge-Project 818 094); Grant sponsor: Hochschuljubiläumsstiftung H-2490.

*Correspondence to: Alexander K. Seewald, Seewald Solutions, Leitermayergasse 33, 1180 Vienna, Austria

Email: alex@seewald.at

Published online in Wiley Online Library (wileyonlinelibrary.com)

DOI: 10.1002/cyto.a.22258

Abstract

Automated microscopic image analysis of immunofluorescence-stained targets on tissue sections is challenged by autofluorescent elements such as erythrocytes, which might interfere with target segmentation and quantification. Therefore, we developed an automated system (Automated REcognition of Tissue-associated Erythrocytes; *ARETE*) for in silico exclusion of erythrocytes. To detect erythrocytes in transmission images, a cascade of boosted decision trees of Haar-like features was trained on 8,640/4,000 areas (15 × 15 pixels) with/without erythrocytes from images of placental sections (4 μm). Ground truth data were generated on 28 transmission images. At least two human experts labelled the area covered by erythrocytes. For validation, output masks of human experts and *ARETE* were compared pixel-wise against a mask obtained from majority voting of human experts. F1 score, specificity, and Cohen's κ coefficients were calculated. To study the influence of erythrocyte-derived autofluorescence, we investigated the expression levels of a protein (receptor for advanced glycated end products; RAGE) in placenta and number of Ki-67-positive/cytokeratin 8-positive epithelial cells in colon sections. *ARETE* exhibited high sensitivity (99.87%) and specificity (99.81%) on a training-subset and processed transmission images (1,392 × 1,024 pixels) within 4 sec. *ARETE* and human expert's F1-scores were 0.55 versus 0.76, specificities 0.85 versus 0.92 and Cohen's κ coefficients 0.41 versus 0.68. A ranking of Cohen's κ coefficient by the scale of Fleiss certified "good agreement" between *ARETE* and the human experts. Applying *ARETE*, we demonstrated 4–14% false-positive RAGE-expression in placenta, and 18% falsely detected proliferative epithelial cells in colon, caused by erythrocyte-autofluorescence. *ARETE* is a fast system for in silico reduction of erythrocytes, which improves automated image analysis in research and diagnostic pathology.

Key terms

erythrocytes; immunofluorescence microscopy; autofluorescence; tissue cytometry; automated image analysis; boosted decision trees of Haar-like features; machine learning; placenta; colorectal cancer

Tissue cytometry refers to automated analysis of digitized microscopic images of stained tissue sections. Following segmentation of the tissue by computer algorithms, qualitative and quantitative analyses of multiple molecules and parameters can be computed on a single cell basis in the tissue context. Tissue cytometry takes into account the strong influence of intact cell-cell and cell-matrix interaction on cellular behavior. In addition, the analysis of large tissue areas enables quantification with statistical significance. Consequently, tissue cytometry is an essential tool not only for research, but also for diagnostic, therapeutic, and predictive medicine (1). Accordingly, a growing number of open-source packages such as Cell Profiler/Broad Institute (2,3) and commercial tools (e.g., TissueQuest by TissueGnostics GmbH, Vienna, Austria; Aqua by HistoRX; InCell by GE Healthcare) are available for automated image analysis of tissue samples (4).

ISAC
International Society for Advancement of Cytometry

In tissue cytometry, detection and measurement of target proteins is based on immunohistochemistry (IHC), which combines antigen-specific primary antibodies and secondary antibodies conjugated to reporter-molecules, and produce a colored precipitate from a chromogenic substrate. Alternatively, in the fluorescence microscopic analysis, antibodies are conjugated to a fluorophor emitting a fluorescence signal. For several reasons, the latter technique is often of advantage in research and diagnostics (5,6). A higher resolution is possible with fluorophore-conjugated antibodies compared to chromogenic substrate precipitates. Multi-antigen imaging enables parallel detection and spatial correlation of several cellular targets. Thereby, the number of targets is mainly limited by availability of fluorophores with nonoverlapping absorption and emission characteristics. In addition, a major advantage is the wide linear dynamic range of fluorophores, which better supports the computed quantitative measurement of parameters in biological specimens than chromogen-based signal-detection that suffers from a more rapid saturation (7,8). This linear quantification of many parameters enabled by automated image analysis is an important improvement to the widely applied qualitative human scoring methods regarding the precision and validity of the results. Human evaluation usually combines the staining intensity of labeled proteins in immunofluorescence microscopic images with the number of stained cells to a nonlinear scoring (9). Human scoring remains semiquantitative and additionally suffers from intra- and interobserver variability (10).

Though there are many advantages, fluorescence microscopy and consequently tissue cytometry is troubled by the phenomenon of autofluorescence. This is caused by either intrinsic fluorescence of cell and tissue components, or induced during fixation or processing of the tissue (11). Intrinsic autofluorescence can originate from porphyrin derivatives such as protoporphyrin IX, a precursor of the heme molecule, which is a major component of erythrocytes. Erythrocytes are present in major blood vessels and microvessels as well as in all histological and pathological tissue samples, but their number per area varies greatly. Erythrocyte-associated autofluorescence can significantly exceed the background fluorescence of the tissue and can interfere with the fluorescence emission of specific targets. Erythrocyte-autofluorescence may be mistaken for a specific fluorescent signal or hide a weak specific signal from the target of interest, and this can influence, for example, nucleus detection, image segmentation, as well as falsify the quantification of the target proteins.

On the contrary, autofluorescence of erythrocytes can also be applied to diagnose and monitor pathological states of erythrocytes. Their fluorescence can be evoked by glycation of proteins, which is the formation of and conjugation with advanced glycated end products (AGEs) (12,13). Enhanced glycation of many molecules is associated with elevated sugar levels (such as glucose) or oxidative stress, and is consequently associated with a variety of pathologic states such as diabetes mellitus (14), neurodegenerated diseases (15), or preeclampsia (16,17).

Autofluorescence induced by fixation can be omitted through changes in the procedures. Moreover, various histochemical techniques for the removal of intrinsic and extrinsic autofluorescence have evolved. However, reduction of tissue autofluorescence has proven very difficult and can destroy major antigens in the tissues. Among the different methodologies used are treatment with ammonia/ethanol or sodium borohydride or quenching of autofluorescence with dyes such as Sudan Black B, Trypan Blue, and others. Photobleaching changes the molecular structure of a fluorophore so that it loses its ability to fluorescence (18–21).

Unfortunately, no general recipe is available for the control of autofluorescence. Certain chemical treatments may even induce erythrocyte-associated autofluorescence (18). Quite often, the autofluorescence of tissues is not eliminated or sufficiently reduced with a single autofluorescence reduction methodology, and therefore combinations of techniques need to be tested in a time-consuming procedure to obtain optimized results for target tissues. Whether the specific pretreatment influences the subsequent target staining has to be determined in a subsequent testing (22). In summary, the elimination of unevenly distributed autofluorescence as associated with erythrocytes cannot be performed with a single standard protocol, requires time for the set up of the best protocol per given tissue and fixation protocol, and adds an additional pretreatment step to the protocol required for immunofluorescence staining. In case multiple antigens are labeled in the same preparation and detected at individual wavelength, the procedure for elimination of autofluorescence has to be performed for any protein and at any individual fluorescence channel needed.

In the context of tissue cytometry, a possibility to circumvent such complicated and time-consuming establishment of protocols to reduce interfering autofluorescence derived from erythrocytes would be the automated detection and exclusion of these cells. Although algorithms for the recognition and classification of erythrocytes in blood (23,24) have been published, the automated detection of tissue-associated erythrocytes has never been described before. Therefore, we developed *ARETE* (Automated REcognition of Tissue-associated Erythrocytes), a computer system, which represents a cascade of boosted decision trees and identifies tissue-associated erythrocytes in digitalized images utilizing their distinctive shape and structure. We developed the system using 8,640 small image areas containing tissue-associated erythrocytes and 4,000 negative samples excised from images of human placental chorionic tissue. Evaluation of *ARETE* was performed by two means. First, on a subset of the training data ($n = 3{,}000$), where *ARETE* demonstrated high sensitivity (99.87%) and specificity (99.81%). Second, we compared the segmentation results returned by *ARETE* with the merged results from manual segmentation of several human experts on 28 randomly selected transmission images from healthy and preeclamptic placental tissues. Manual segmentation by humans is usually regarded as being the gold standard for validation purposes, although it is affected by intra- and interexpert variability. In the pixel-based comparison, F1 score and specificity of *ARETE*

and single experts were compared to the merged experts' values. A ranking of Cohen's κ coefficient (0.41 vs 0.68) (25) by the scale of Fleiss (26) indicated good agreement between *ARETE* and the human experts.

Finally, we give two examples of how the erythrocyte-associated autofluorescence can influence the results of automated image analysis in research and eventually in digital pathology.

In placenta, we quantified the expression of the Receptor for Advanced Glycated End products (RAGE). Because soluble AGE-modified molecules can activate the receptor for AGEs on various cell types, thereby promoting chronic inflammatory states, RAGE is a putative target of anti-inflammatory treatment. Therefore, the levels of RAGE expression in healthy and diseased tissues of various origins including placenta are of interest (27). As expected, the automated analysis of RAGE expression using immunofluorescence microscopy was impaired by autofluorescence of erythrocytes.

In colon cancer tissue, the proliferation rate of cancer cells influences the onset of metastasis, disease-free and overall survival. The metastatic potential of the tumor may be evaluated by assessing the expression of the proliferation marker Ki-67 in cytokeratin 8-positive epithelial cancer cells. We exemplify the falsification of the number of Ki-67-positive cells by erythrocyte-associated autofluorescence.

Overall, *ARETE* offers several advantages compared with a chemical control of autofluorescence. *ARETE* generates the "erythrocyte mask" within 4 seconds from the transmission image. Chemical protocols usually require several hours for execution and even longer for their establishment. Executed on transmission images, an interference of the erythrocyte-detection with the specific staining in any of the fluorescence channels does not exist. Acquisition time for transmission images is short (1 msec) and therefore does not lead to bleaching of fluorescence and subsequent reduction of quantified pixel-intensity. As it operates on transmission images, the dedication of any fluorescent channel for the detection of erythrocytes via specific antigens is also unnecessary.

Materials and Methods

Immunofluorescence Staining

Tissue sections from human placenta and colon have been used in this study. Samples were derived from collaborations with the Department of Pathology at the Medical University Vienna, Austria, and all studies were approved by the ethic commission of the Medical University Vienna. If not stated otherwise, all chemicals were obtained from Sigma-Aldrich (St. Louis, MO). The formalin-fixed paraffin-embedded tissues were sectioned (4 μm) and mounted on Microscope slides (Menzel GmbH, Braunschweig, Germany).

Human placenta. For automated analysis of expression levels of placental proteins in healthy and diseased human placental chorionic tissue, we have recently published a system for automated detection of total placental chorionic tissue area and additional segmentation of the multinucleated syncytiotrophoblast area, which is the surface cell layer of the villi interacting with maternal blood (28). The segmentation algorithm is based on the detection of cytokeratin 7, a specific cytoskeletal component of the syncytiotrophoblast, using immunofluorescence microscopy. After segmentation, staining intensities of proteins of interest per total chorionic tissue area, syncytiotrophoblast area, or total tissue area minus syncytiotrophoblast area (i.e., stromal tissue area) can be computed. Molecules of interest may be proteins such as the receptor for advanced glycation endproducts (RAGE) suspected to be involved in the development of a pregnancy-specific disease [preeclampsia; (29)] or molecules such as gamma smooth muscle actin (gsm-actin), which help to further classify the tissue structures (30).

Labeling of proteins was performed on placental tissue sections from healthy as well as preeclamptic placentas by indirect immunohistochemistry using specific primary and fluorophore (Alexa Fluor-488, Alexa Fluor-568, and Alexa Fluor-647)-conjugated secondary antibodies. After deparaffinizing and rehydrating, antigen retrieval was done by boiling samples for 15 min in 0.01 M citrate buffer, pH 6.0. Following permeabilization and blocking with 5% (w/v) goat serum (Dianova GmbH/Jackson ImmunoResearch) plus 0.05% saponin in phosphate-buffered saline (PBS; placenta blocking buffer), sections were incubated consecutively with the following antibodies diluted in placenta blocking buffer for 1 h at room temperature with intense washing steps in between: rabbit anti-human RAGE (N-300, Santa Cruz Biotechnology, Santa Cruz, CA) diluted 1:50, Alexa Fluor 568 goat anti-rabbit (Invitrogen Molecular Probes/Life-Technologies, Paiseley, UK) diluted 1:1,000, mouse anti-human cytokeratin 7 (clone OV-TL 12/30, DaKo, Denmark) diluted 1:100, Alexa Fluor 647 goat anti-mouse (Invitrogen Molecular Probes/Life-Technologies, Paiseley, UK) diluted 1:1,000, mouse anti-actin (MAb Clone B4, MP Biomedicals, Aurora, OH) diluted 1:250 and Alexa Fluor 647 goat anti-mouse (Invitrogen Molecular Probes/Life-Technologies) diluted 1:1,000.

Human colon. Antigen retrieval in colon tissue sections was performed by boiling samples for 20 min in 0.05% (w/v) citraconic anhydride. Following permeabilization in PBS/Tween 0.2% (w/v) and blocking with 5% (w/v) goat serum (distributor Dianova GmbH, Hamburg, Germany; formerly Jackson ImmunoResearch, West Grove, PA, USA) plus 0.05% Tween in PBS (colon blocking buffer), sections were incubated in parallel with mouse anti-human Ki-67 (clone MIB-1, DaKo, Denmark) diluted 1:50 in colon blocking buffer and rabbit anti-human keratin 8 (clone EP1628Y, Thermo Fisher Scientific, Fremont, CA) diluted 1:200 in colon blocking buffer for 1 h at room temperature. After washing, sections were incubated in parallel with Alexa Fluor 647 goat anti-mouse (Invitrogen Molecular Probes/Life-Technologies) diluted 1:1,000 in blocking buffer and DyLight 549 goat anti-rabbit (Vector Laboratories, Burlingam, CA) diluted 1:100 in blocking buffer for 1 h at room temperature.

In all samples, 4′,6-diamidino-2-phenylindole (DAPI; Roche Diagnostics GmbH, Vienna, Austria) was applied at 0.2 μg/ml PBS for 10 min at room temperature to visualize cell

nuclei. Control stainings were performed omitting the primary antibodies. After washing, slides were mounted with Fluoromount G (SouthernBiotech; Burmingham, AL).

Image acquisition

Tissue sections were acquired using a TissueFAXSplus tissue cytometer (TissueGnostics GmbH) equipped with epifluorescence optics and a Plan NeoFluar objective (20×/NA 0.5; Zeiss, Oberkochen, Germany). The following filter sets (Chroma 49000 series filter sets) were used: DAPI (350-nm excitation, 400-nm dichroic, 460-nm emission), FITC/Cy2 (470-nm excitation, 495-nm dichroic, 525-nm emission), mCherry/TxRed (560-nm excitation, 585-nm dichroic, 630-nm emission), and Cy5 (620-nm excitation, 660-nm dichroic, 700-nm emission). The monochrome camera of the TissueFAXSplus instrument was used to acquire grayscale images of all samples. To ensure correct focus, we took all images were automatically on five different *z*-levels with a 2 μm interval. The *z*-stacks were merged into one critically sharp image using extended focus, an integrated feature of the software. Fluorescence and corresponding transmission images were acquired and stored with lossless compression in PNG format. Automated identification and segmentation of placental chorionic villi into the syncytiotrophoblast and the stromal core was performed via cytokeratin 7-positive trophoblast cells as published (28). Cell segmentation of colon sections in order to identify single cells positive for Ki-67 staining was done by TissueQuest software version 4.0 based on nuclei detection (TissueGnostics GmbH).

Generation of ground truth data

The ground truth dataset was obtained by randomly selecting 28 independent transmission images (fields of view) from healthy and preeclamptic placental tissue sections. Part of such an image is shown in Figure 3a, demonstrating the distinctive shape of erythrocytes. At least two trained personnel (human experts) inspected these fields of view and manually marked up the area covered by erythrocytes in the transmission images using a Wacom Graphics Tablet (WACOM Europe GmbH, Germany) and the image-processing program Adobe Photoshop CS 4.0 (Adobe Systems Inc., USA). An example for a manual markup of one expert is given in Figure 3b. The instruction given was to "cover the erythrocyte-area in the image." On a limited set of images ($n = 8$), the instruction was "label every single erythrocyte with a dot of 8 pixel radius."

Preparing the training set

ARETE is a machine-learning-based solution that was trained on 8,640 samples containing erythrocytes (e.g., see Fig. 2c) and 4,000 samples of nonerythrocyte areas extracted from transmission images of human placental and colon tissue sections. To speed up the cut out process of true positives (TP) as well as true negatives (TN) from images, the small tool *ARETE*-CUT was implemented. Erythrocytes (=TP) were semiautomatically cut out just by clicking on them (assuming a fixed size of 15 × 15 pixels). Additionally, it was used to select tissue areas (various sizes) that did not contain erythrocytes (=TN).

Training of *ARETE*

The algorithm *ARETE* is a cascade of boosted decision trees (31). The training process builds a cascade that consists of a set of weak classifier augmented by an adaptive boosting technique [AdaBoost; (32)] where each subsequent classifier trains on a reweighted training set. The cascade of weak classifiers ensures fast execution—the classifier must be run on every possible window of the image at multiple resolutions—whereas the boosting step ensures sufficiently good performance of the ensemble of weak classifiers at each cascade level.

The extended set of Haar-like features (exemplified in Fig. 2c) described by (33) was employed. Haar-like features enable the fast extraction of several hundreds of thousand features from small rectangular areas by computing the difference between the sums of the pixels within two or three aligned adjacent rectangular regions.

Application of *ARETE* on tissue sections

In the detection phase, the previously trained cascade was employed on transmission images of tissue samples. Rectangles were moved at different scales over the input image of a given tissue section acquired using microscopy (Figs. 2a and 2b) and each window was processed by the cascade of boosted trees (Fig. 2c). If a window was classified to contain an erythrocyte, a circle with a radius of eight pixels was inscribed. Locations were clustered and combined with nonmaximum suppression and neighbor-filtering. Additionally, images were rotated four times by 90° and analyzed in parallel, yielding four independent estimates for each image that were combined using logical OR. This procedure increased the accuracy of the detection by about 20%, because uneven illumination can introduce a gray-scale gradient that is also learned by the model. This gradient may differ on other instrument setups; however, this step ensures a stable detection even for other gradients. In this way, an output mask (Fig. 2d) was created, where each erythrocyte was indicated as a set of pixels with an intensity value greater than 0. This mask contained information such as the location and the area covered by the erythrocytes and enabled the exclusion of these tissue areas from further analysis in corresponding images acquired in fluorescence channels (Figs. 2e and 2f). As an alternative application, a specific analysis of the erythrocyte features can be considered such as erythrocyte-covered area, autofluorescence intensity-level, and so on.

Validation of *ARETE*

First, sensitivity and recall/specificity of the performance of *ARETE* on a subset ($n = 3{,}000$) of the training set was computed (see Table 1). High sensitivity and specificity were obtained.

Afterward, human expert masks of 28 transmission images of placental tissue sections were compared against each other using majority voting (MV) for each FOV. Pixels lying within all individual human expert markups were defined as TP, pixels obtained from less experts were either false positives (FPs) or false negatives depending on the majority vote at that pixel. We computed specificity, as well as the balanced F1 score (based on the effectiveness measure E from reference 34), which is a weighted average of precision and recall/sensitivity

Table 1. Summary of all computed statistical measures during the evaluation of *ARETE*

	PERFORMANCE ON THE TRAINING-SET				
Recall/Sensitivity	0.9987				
Specificity	0.9981				
Medians of	Human experts				*ARETE*
Precision	0.63				0.52
Recall/Sensitivity	0.88				0.60
F1 Score	0.76				0.55
Specificity	0.92				0.85
Cohen's κ coefficient [(25) Cohen, 1960]	0.68				0.41
Landis and Koch (22)	No: 0–20	Slight: 20–40	Fair: 40–60	Substantial: 60–80	Almost perfect: 80–100
Fleiss (23)	Poor: 0–40		Fair to good: 40–75		Excellent: 75–100

for the area-wise agreement between individual human experts and Cohen's κ coefficient (25) to assess inter-rater agreement. These statistical measures are defined as follows:

$$\text{specificity} = \frac{\text{tn}}{\text{tn} + \text{tp}},$$

$$\text{precision} = \frac{\text{tp}}{\text{tp} + \text{fp}},$$

$$\text{recall/sensitivity} = \frac{\text{tp}}{\text{tp} + \text{fn}},$$

$$\text{F1} = 2\times\frac{\text{precision}\times\text{recall}}{\text{precision} + \text{recall}}, \text{and}$$

$$\kappa = \frac{Pr(a) - Pr(e)}{1 - Pr(e)}$$

Subsequently, we compared the erythrocyte area detected automatically using *ARETE* in a pixel-wise manner with the majority voted mask obtained from markups of the experts. This logical operation combines two different masks by creating a new mask containing all pixels of both individual experts. Cohen's κ coefficient was classified according to the scale of either Landis and Koch (35) or Fleiss (36).

Results

Human placental chorionic tissue was used to develop the automated erythrocyte detection system (*ARETE*). This tissue represents the interface between maternal and fetal blood circulation, and consequently high local numbers of erythrocyte are found (Figs. 1a and 1b). Mature erythrocytes appear as circular disks, biconcave in profile, and are a-nuclear with an average diameter of about 7.5 μm. The size and shape of erythrocytes gives them a characteristic appearance in transmission microscopic images that allows for their self-evident identification by the human observer (Figs. 1a and 1b). When investigating expression levels of various placental proteins using immunofluorescence microscopy, we observed that the erythrocytes contained in fetal vessels (Fig. 1b) exhibited

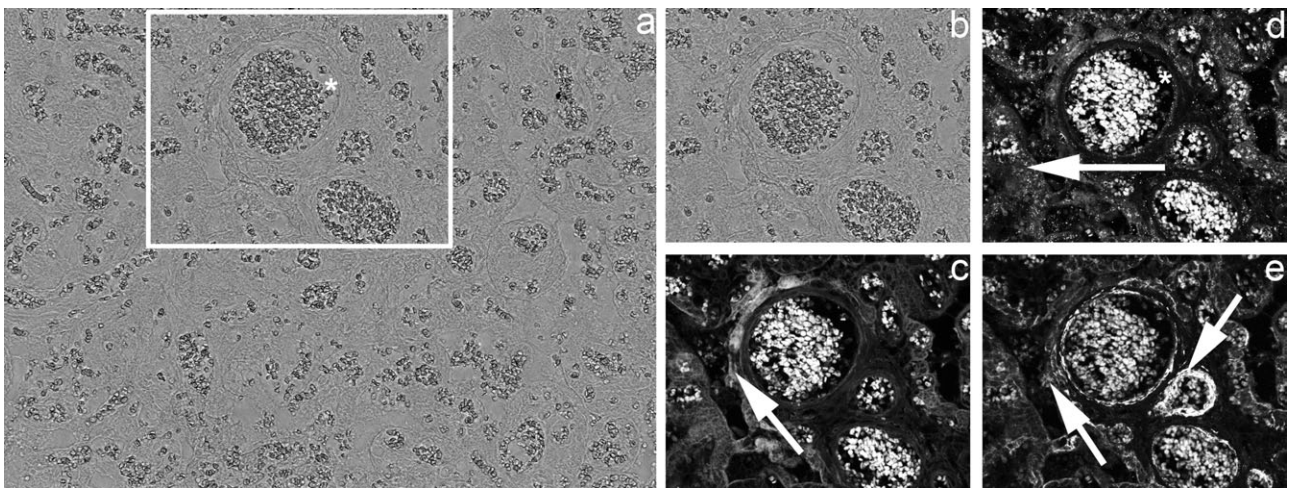

Figure 1. Transmission image (a) of a paraffin section of human placental chorionic tissue where multiple erythrocytes are visible (dark gray structures, indicated by asterisks). (a) subregion of this transmission image (b) with corresponding images derived from three individual fluorescence channels (c) 470-nm ex/525-nm em, (d): 560-nm ex/630-nm em, and (e): 620-nm ex/700-nm em). Arrows indicate the target staining [cytokeratin 7 (c), receptor for advanced glycated end products (RAGE) (d), cytokeratin 7 and gamma smooth muscle-actin (e)], whereas asterisks indicate the positive staining contributed by erythrocytes.

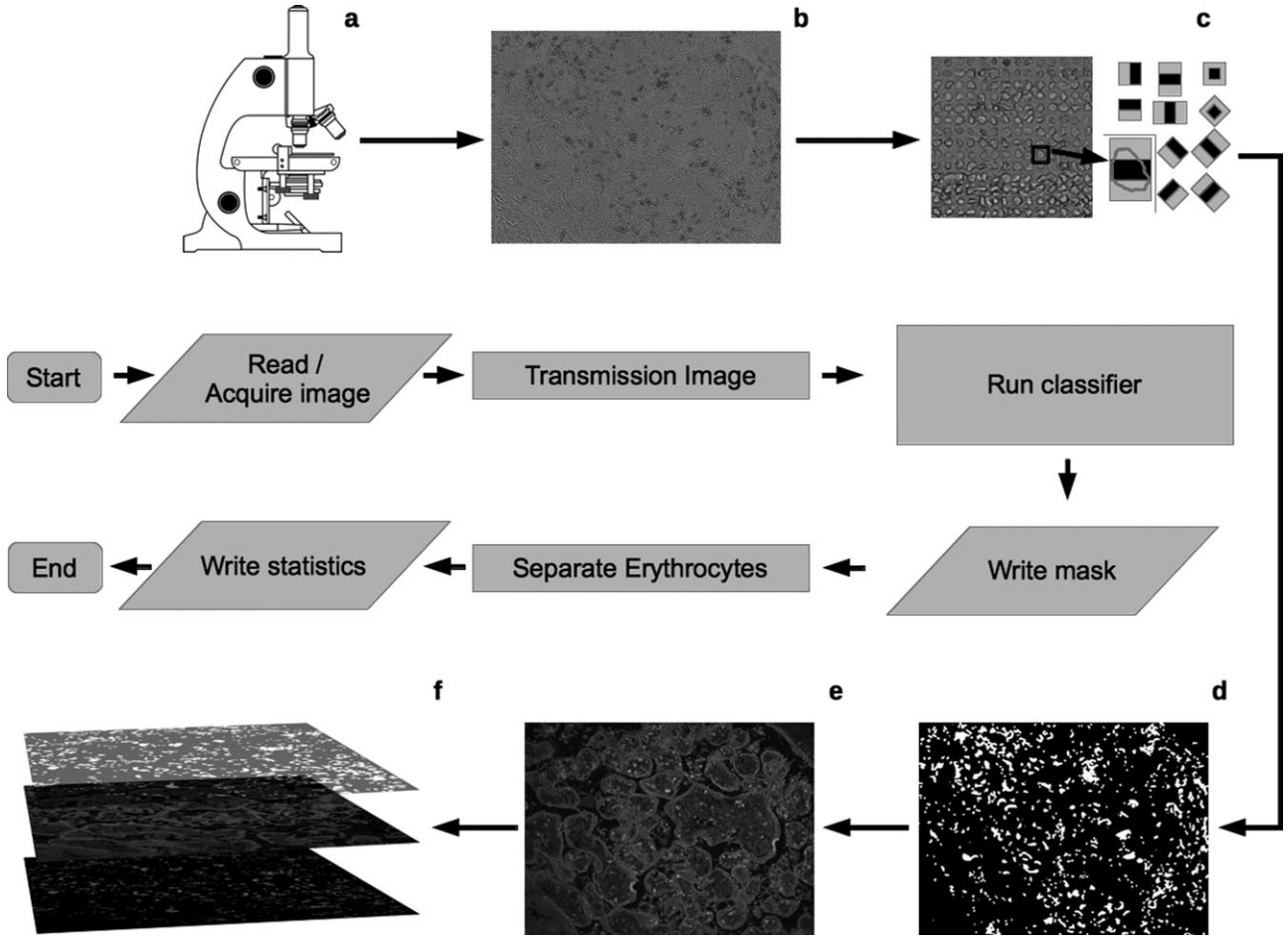

Figure 2. Schematic workflow of *ARETE*. (a,b) After co-acquisition of a transmission image corresponding to fluorescence images exhibiting autofluorescence, (c) a cascade of boosted decision trees of Haar-like features previously trained on 8,640 positive samples and 4,000 negative samples for erythrocytes is employed to classify small rectangular subregions of the transmission image resulting in a binary mask (d). This mask can be combined with corresponding fluorescence channels (e, f) to enable in silico subtraction or extraction of erythrocyte-associated autofluorescence.

bright autofluorescence at 470-nm ex/525-nm em (Fig. 1c), at 560-nm ex/630-nm em (Fig. 1d) as well as 620-nm ex/700-nm em (Fig. 1e). Their local fluorescence intensity values often exceeded the intensity values of the antigens under investigation such as cytokeratin 7-Alexa Fluor 488 (Fig. 1c), RAGE-Alexa Fluor 568 (Fig. 1d), or a combination of cytokeratin 7 and gsm-actin-Alexa Fluor 647 (Fig. 1e). On the basis of this observation, we conclude that erythrocyte-associated autofluorescence could significantly influence and falsify automated segmentation and quantification of proteins (see also Fig. 4).

Automated detection of erythrocytes in paraffin-embedded tissue sections

To minimize the local erythrocyte-associated autofluorescence in the context of tissue cytometry, we sought after an automated erythrocyte detection tool that would enable us to reduce or eliminate these cells in-silico. To overcome the limitations owing to restricted availability of fluorescence channels on the microscopes available in different laboratories, time-consuming execution of complex multi-staining protocols, and determination of specificity of antibodies against erythrocyte-specific antigens (such as CD233), we devised *ARETE* on transmission images co-acquired with immunofluorescence-stained images (see Fig. 1a). As the shape and size of erythrocytes is easily identified by humans, we thought to train the computer to identify these cells as well.

The principal workflow of *ARETE* is depicted in Figure 2. Microscopic transmission images (Fig. 2a/b) serve as input enabling the localization of erythrocytes. We used a machine learning system employing a cascade of boosted decision trees and trained it on 8640 small image areas (15×15 pixels) containing tissue-associated erythrocytes (some of them indicated in Fig. 2c) and 4,000 erythrocyte-negative tissue areas. When applying *ARETE* on transmission images derived from tissue sections, the trained cascade was used to detect erythrocytes within small rectangles moved over the input mask. If an erythrocyte was detected, a circle with a

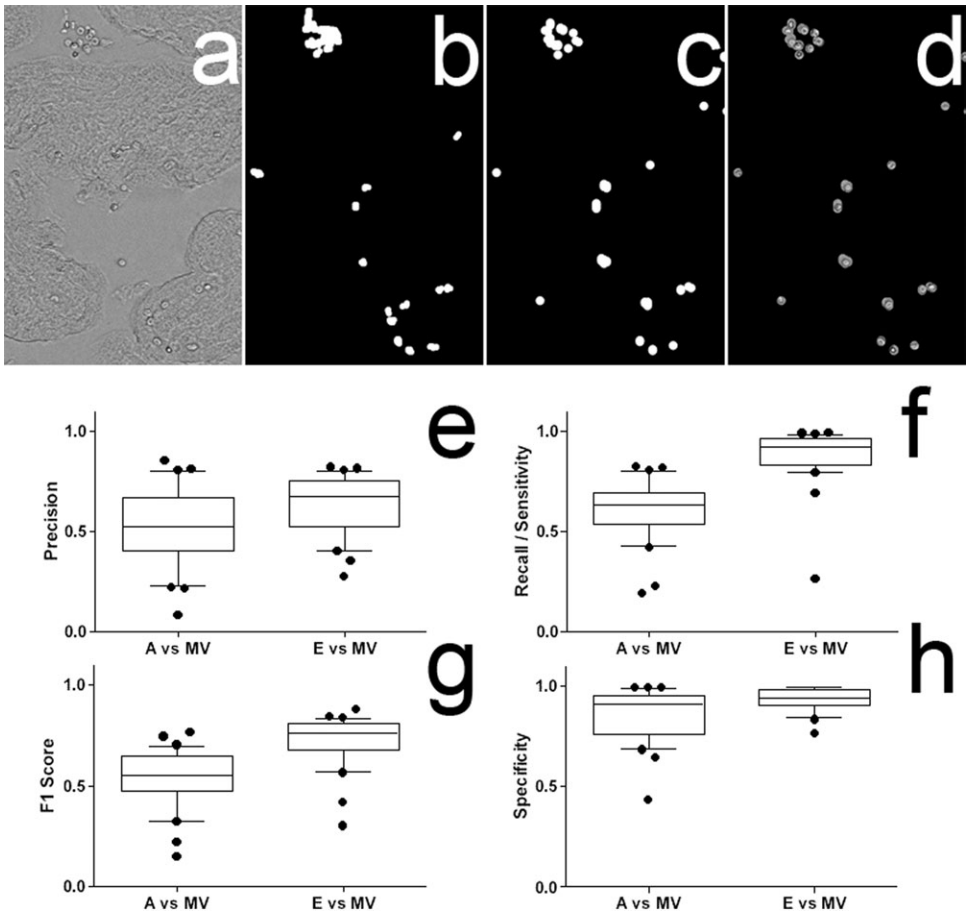

Figure 3. The upper part shows a subregion of a transmission image (a) with the corresponding manual expert markup (b), *ARETE*'s output mask (c), and a mask containing the extracted erythrocytes (d). This montage also illustrates the uncertainty because of different markups techniques of *ARETE* and the human expert. Beneath, a quantitative comparison of the 28 output masks of *ARETE* with ground truth data generated by at least two human experts is shown in e—g. Masks derived from 24 images were compared by computing the measures precision, recall/sensitivity, the derived F1 score, and specificity. The whiskers show the 10% and 90% percentiles. Outliers are plotted as black dots. The line within the box-plot indicates the median. A (*ARETE*), E (single human expert), MV (Majority voting of experts), F1 score (harmonic mean of precision and recall).

radius of 8 pixels was inscribed. Though a circle only approximates the individual shape of an erythrocyte, a fact that may contribute to FP pixel resulting from erythrocytes that differ from the shape of a circle, it allowed for a much faster processing (4 sec/image) compared to additional analysis of each window to detect the exact shape of the erythrocyte (up to 12 sec/erythrocyte).

ARETE results in a versatile binary output mask (Fig. 2d), which can serve to subtract areas containing autofluorescent erythrocytes from corresponding fluorescence images (Figs. 1e–1f).

Specificity and sensitivity of *ARETE* on a subset of the training set

To evaluate the performance of the trained cascade, we computed the specificity and sensitivity on the training set. A high score assures that the employed features learned the patterns of the target structure (erythrocytes). In both the cases, the values were close to 1 (Table 1).

Comparison of erythrocyte-masks delivered by *ARETE* and human experts

In many fields, the humans remain the main reference for the capability of any algorithm (37). This "gold standard" derived from human markups was also set to be the upper performance limit of *ARETE*. However, in the evaluation of algorithms for medical image segmentation, it has to be kept in mind that the manual segmentation by humans is affected by intra- and interexpert variability (10). To account for the known inter-observer differences, at least two human experts independently inspected 24 transmission images derived from placental tissue and marked the areas covered by erythrocytes as described in *Materials and Methods* section. Following a pixel-wise comparison of single expert masks against a majority voted (MV) mask, we calculated several measures such as precision, recall/sensitivity, the F1 score that combines both measures, specificity, and Cohan's κ coefficient (25) to estimate the inter-rater agreement of the human experts.

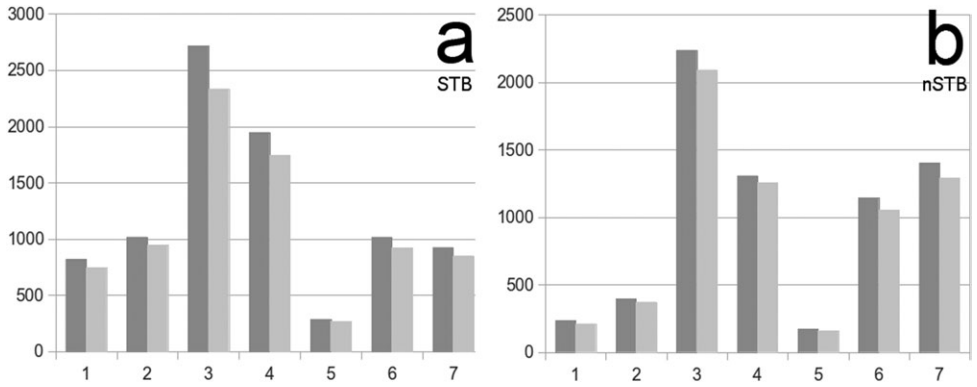

Figure 4. Effect of in silico removal of erythrocytes by *ARETE* on the automated quantification of expression levels of the receptor for advanced glycated end-products (RAGE) in human chorionic tissue. Seven regions of placental tissue sections (1—7, each composed of 9 × 9 images) were segmented based on cytokeratin 7 staining (16) to obtain areas corresponding to the multinucleated cell-type syncytiotrophoblast (STB; a) and all other cells contained in the stromal core of the chorionic tissue (nSTB, b). After this segmentation, the RAGE-derived fluorescence intensities values associated with these individual areas (STB, nSTB) were calculated and plotted prior (dark gray) and after (light gray) in silico removal of autofluorescence derived from erythrocytes by *ARETE*. Subtraction of the erythrocyte mask generated by *ARETE* from the original fluorescence images used to calculate RAGE expression levels (16) decreased (light gray) of RAGE expression in the syncytiotrophoblast (STB) by 7—14% (a) and by 4—10% in the stromal core associated cells (nSTB; b) compared with the original unmodified images (dark gray).

Likewise, the *ARETE*-output masks, exemplified in Figure 3c, were compared pixel-wise with the majority voted (MV) mask. Visual comparison of the returned erythrocytes mask with the transmission images indicated good agreement (see montage in Figs. 3a–3d). A quantitative comparison over all 28 images between *ARETE* and experts is shown in Figures 3e–3h, depicting precision (Fig. 3e), recall/sensitivity (Fig. 3f), the F1 score that combines both measures (Fig. 3g), and specificity (Fig. 3h). We calculated Cohen's κ coefficient and ranked the agreement between *ARETE* and the human experts according to the scale introduced by either Landis and Koch (35) or Fleiss (36). All statistical results are summarized in Table 1.

With respect to specificity (indicating the rate of pixels falsely classified as belonging to erythrocytes), *ARETE*'s median performance approximated the human performance well. When measuring precision and recall/sensitivity as well as the derived F1 score, the measures derived from comparing *ARETE* with human experts were lower than for inter-observer agreement.

The agreement of *ARETE* with human experts and the inter-rater agreement were also assessed via Cohen's K coefficient. When classifying these values according to the scale introduced by Landis and Koch (35) from 0 (poor) to 1.0 (almost perfect), *ARETE* achieved a moderate (Cohen's κ coefficient = 0.41) agreement, which is one class worse compared to human experts, which were classified as having substantial agreement (Cohen's κ coefficient = 0.68). In contrast, when applying the scale of Fleiss (36), both *ARETE* versus human experts agreement and human inter-rater agreement were regarded as fair to good.

To assure comparability of the round masks generated by *ARETE* with the expert's ground truth masks, we additionally compared *ARETE* with a set of eight images that were marked up by four experts using the same approach as *ARETE* (fixed circle radius of 8 pixels). No significant change in the above measures was observed (data not shown).

Application of *ARETE*—Exemplifying the effect of erythrocyte-associated autofluorescence on automated image segmentation and quantification

Human placenta. To analyze protein expression patterns in human placental chorionic tissue, we recently introduced an image segmentation algorithm (28). This approach identifies a multinuclear epithelial cell type (syncytiotrophoblast) via cytokeratin 7 staining. Subsequently, it also allows for identification of total chorionic tissue area, which is completely covered by the syncytiotrophoblast and enables discrimination of the syncytiotrophoblast cell area from other cell types in the so-called stromal core of the chorionic tissue (fetal endothelial cells, macrophages, fibroblasts, and other cell types). To exemplify the significant influence of erythrocyte-associated autofluorescence on segmentation and subsequent protein quantification within the two segmented tissue areas of the chorionic placental tissue (syncytiotrophoblast and stromal core), seven regions (each 9 × 9 images) of placental chorionic tissue were analyzed for the expression level of the protein RAGE either in the presence of erythrocytes or after erythrocyte in silico removal by *ARETE*. As can be seen in Figure 4, erythrocyte-associated autofluorescence adds to the level of quantitated RAGE protein in both the syncytiotrophoblast (Fig.4a, 7–14%) and the cells found in the stromal core (Fig. 4b, 4–10%). It can be deduced from the figures that the individual placental samples contained varying amounts of erythrocyte-associated autofluorescence, which does not allow for the subtraction of a "mean value of erythrocyte-associated autofluorescence" from all regions analyzed, but requires image-specific erythrocyte removal.

Human colon. In other tissues such as colon, even the presence of small numbers of erythrocytes can falsify results. Lower cellular proliferation in colon cancer is associated with advanced disease stage and a shorter disease-free survival, in-

dependently of adjuvant chemotherapy received by some patients (38). To improve diagnosis and prognosis, the detection of single cells or small groups of epithelial cells in colon cancer tissue and their analysis for expression level of proliferative marker Ki-67 can indicate the metastatic potential of the tumor. We stained colon tissue sections with antibodies specific for epithelial cell antigens (Cytokeratin 8, CK8) and proliferative marker Ki-67. Nuclei were detected using DAPI. For evaluation, we made use of existing commercial software tools based on cell-segmentation after nuclei detection (TissueQuest/TissueGnostics GmbH). In Figure 5a, the epithelial cells within the tissue have been visualized through CK8 staining. Erythrocytes exhibit bright autofluorescence, which is visible in the CK8 channels (Fig. 5a) and also in the DAPI detecting channel that is used to identify cells and in the Ki-67 staining that identifies proliferating cells. On the basis of the DAPI staining, the automated segmentation outlined all cells expressing the epithelial marker CK8 in green and those cells that were positive for CK8 in red, and in addition demonstrated Ki-67 expression (Fig. 5b). Within this area, 479 cells positive for both markers were automatically counted in the presence of erythrocytes. However, erythrocytes localized in this image (some indicated by arrows) falsified the result. Following their detection by *ARETE* and subsequent in silico removal, the number of CK8/Ki-67-positive cells was reduced significantly by 18% to 393 (Fig. 5c). For better illustration, the area in the square is magnified in Figures 5d–5g. Because of the autofluorescence of erythrocytes in the DAPI (Fig. 5g) as well as CK8 (Fig. 5f) and Ki-67 (Fig. 5d) channel, erythrocytes contributed significantly to a number of cells detected as being double-positive for CK8 and Ki-67. A dramatic reduction from 7 to 2 double-positive cells was detected in this area after in silico removal of erythrocytes (compare Figs. 5d and 5e). This computed result was confirmed by human expert visual inspection.

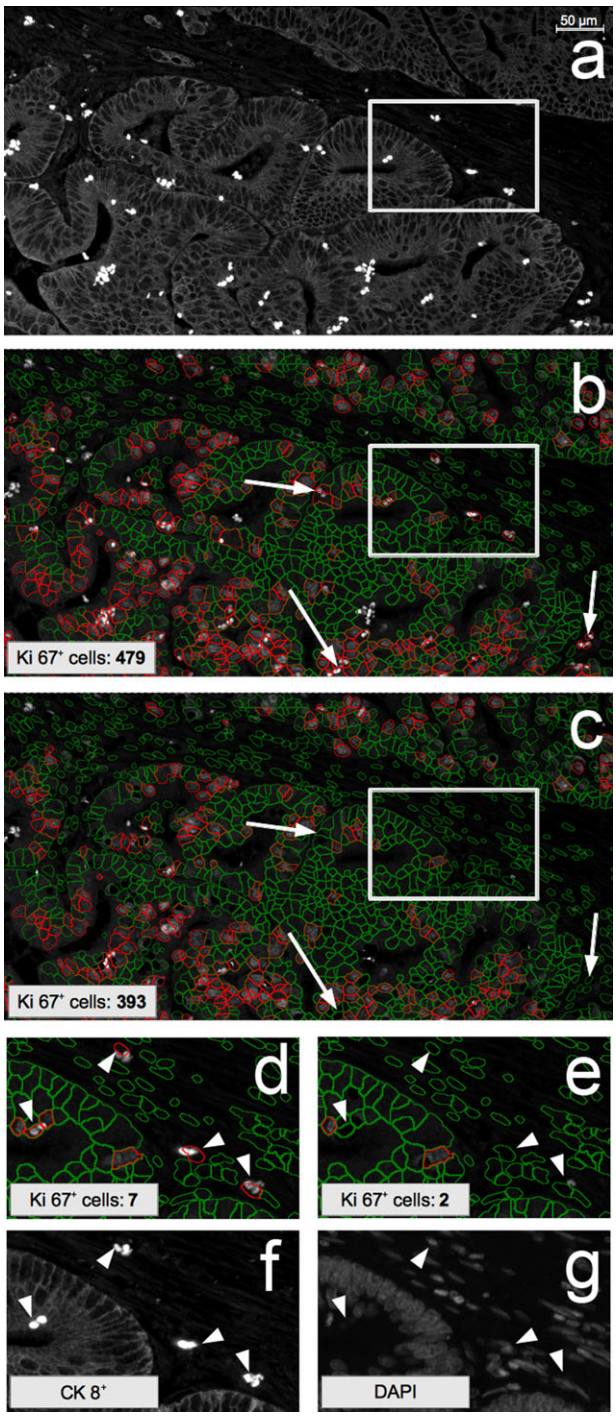

Discussion

Advantages of *ARETE* over histochemical reduction of autofluorescence

Erythrocytes contained within tissues can significantly influence automated protein quantification. Indeed, we demonstrate by the application of *ARETE* that in immunofluorescence-stained tissues, erythrocyte-autofluorescence falsely increased apparently RAGE expression by 4–14% in placenta, and the number of proliferative epithelial cells in colon cancer by 18%. In principle, it is possible to control autofluorescence by chemical treatments of samples via at least three different strategies. First, extraction of the autofluorescent constituent by dissolution using, for example, ammonia-ethanol; second,

Figure 5. Effect of in silico removal of erythrocytes by *ARETE* on the automated detection of cytokeratin8 (CK8)/Ki-67 double positive cells in human colon cancer tissue. A paraffin section of the tissue was processed using immunofluorescence microscopy to detect epithelial cells (CK8+; a) that also expressed the proliferation marker Ki-67. Nuclei were stained with DAPI. Following automated image acquisition, cells were segmented via nuclei detection using Tissue Quest 4.0. All detected cells are outlined in green, those expressing CK8 as well as Ki-67 are outlined in red. (a) shows the CK8 positive epithelial cells. This image was processed without (b) and with (c) erythrocyte removal by *ARETE*. In (d), the autofluorescence of erythrocytes leading to false positive Ki-67 cells in the CK8 channel is exemplified. Application of *ARETE* reduced the amount of Ki-67 positive cells by 18%. The arrows in (b,c) indicate where cell-touching erythrocytes caused false-positive Ki-67 cells. A rectangular subregion is shown magnified in (d) and (e) with the corresponding fluorescence channels for CK8 (f) and DAPI (g). In this subregion, the arrowheads point out false-positive cells ($n = 5$).

by chemical modification of the fluorochrome by, for example, borohydride (in case of aldehydes), and third, by masking the autofluorescent structures by appropriate stainings, for example, Sudan black B (18). Though these strategies for the elimination of autofluorescence prior to (immuno-)fluorescence microscopy exist, the study from Baschong (18) indicated that a general recipe for the (chemical) control of autofluorescence in different samples is not available. For example, borohydride, which is a confirmed requisite for autofluorescence control in glutaraldehyde-fixed tissue (39), had a paradoxical effect in formaldehyde-fixed tissue, where it induced bright fluorescence in erythrocytes. Therefore, success in reducing autofluorescence with chemical reagents always requires a tactical approach with the choice of the appropriate reagent(s) (single or combined) for the specific tissue type, fixation medium, processing technique, and wavelength of excitation light. In conclusion, the establishment and execution of any protocol for autofluorescence removal is time consuming. In addition, interference of the developed protocol with the immunodetection of a protein under investigation needs to be tested. Overall, the established protocol has to be re-evaluated any time a new fixation technique, tissue, or antigen is under investigation.

To circumvent these troubles, we introduced *ARETE*, which is the first prototype of a detection system operating on transmission images to detect erythrocytes in tissue sections. In contrast to the time-consuming protocols for chemical treatments, *ARETE* generates the "erythrocyte mask" from the transmission image within 4 sec/image. An interference because of the erythrocyte detection with the specific staining in any of the fluorescence channels does not exist as the algorithm works on transmission images. Because of the short acquisition time for transmission images (1 msec), their generation does not cause bleaching/reduction of specific fluorescence signals. As it operates on transmission images, the dedication of any fluorescent channel of the microscope for detection of erythrocytes via specific antigens is unnecessary and allows for using all microscope channels for detection of proteins of interest.

Performance of *ARETE*

Speed. *ARETE* is based on a cascade of boosted decision trees of Haar-like features, which is a machine-learning approach able to handle a variety of complex structures such as pedestrians (40), faces (33), hand gestures (41) and clathrin-coated pits (42). In tissue cytometry, one main idea is to investigate large areas of the tissue instead of single images in order to obtain enough data for statistically significant evaluation. Therefore, rapid processing is an important issue. Boosted decision trees of Haar-like features allow for fast high-throughput analysis compared to other approaches used to segment bright-field images such as cascades of support vector machines (43). Support vector machines need all input features for classification and therefore compute all features for each patch instead of just a small number related to tree size as the decisions trees used for *ARETE*. Because of this, the support vector machines detection system is likely to be several orders of magnitude slower than *ARETE* [no data on runtime is given in (43)].

Validation of *ARETE*

Evaluating the output of *ARETE* is nontrivial as a variety of factors influence the validation. Compared to other approaches (24) where the evaluation of erythrocyte detection and classification was done on an object level, we had to deal with a pixel-wise comparison. Because of the small shape and huge number of erythrocytes in the images derived from placental tissue sections, it is not feasible to delimit the area of each single cell exactly by hand while generating a ground-truth markup. Our experts used the pen tool of Adobe Photoshop and delimited areas of erythrocytes instead of delineating every single cell. This however results in a fuzzy ground-truth dataset. Additionally, *ARETE* inscribes circles at each detected erythrocyte location, an approximation that takes about 4 sec/image. Detecting the real shape was originally tested, but turned out to slow down the process tremendously (12 sec/erythrocyte). Detecting true shapes of erythrocytes in such huge microscopic images (approximately 91.2 megapixel) with several thousands of erythrocytes was therefore sacrificed for the sake of speed.

Regardless of the process that detects erythrocytes, the result is always a pixel-based area mask that marks regions containing erythrocytes. In case of *ARETE*, the detected output mask is composed of the predicted erythrocytes location with approximate average sizes of erythrocytes at the given image resolution. In case of the biological experts, most of the output masks were created using paintbrushes of fixed size corresponding to approximate average sizes of erythrocytes. We conclude that both output masks are comparable as their output depicts the same information albeit attained through different means. To confirm this, we generated additional ground truth data, where the experts labeled erythrocytes in the same way as *ARETE* did, namely by placing a circle with a radius of 8 pixels on each erythrocyte. This slightly different modus of generating the ground truth did not significantly change the results of the validation of *ARETE* versus human erythrocyte detection in tissues.

A visual comparison of the returned erythrocytes mask with the human expert markups suggested good agreement (Figs. 3a–3d). In addition, as has been noted by others recently, a ground truth for medical image segmentation generated by humans is influenced by intra- and interexpert variability (44). Merging of the ground truth data of several experts to reduce intervariability is not trivial and furthermore raises the problem of disposition of various human experts to label many events on multiple images.

The median of the recall of *ARETE* was lower than that of single experts compared to ground truth data (Experts 0.88 vs *ARETE* 0.60). This can be related to two observations. First, erythrocytes exhibit various shapes depending on age and pathological settings as described first by Bessis (45). We assume that even the large training set of more than 8,000 erythrocytes did not fully cover all possible variations. Second, *ARETE* performed weak on areas containing large vessels with

a very high number and density of erythrocytes. High density may also alter the shape of the erythrocytes. In practice, it is currently feasible to exclude such vessels from acquisitions by intelligent drawing of regions of interests, whereas exclusion of single erythrocytes next to other cells is not practicable.

To overcome this issue, retraining the system with more erythrocytes—such as erythrocytes selected from difficult areas or erythrocytes training sets selected by many humans to exclude any bias in the selection of erythrocytes—could solve that problem. Indeed, sensitivity and specificity of *ARETE* on a subset of the training set was very high (see Table 1), indicating that almost all of the (single) erythrocytes selected for the training are perfectly well detected. Banko (46) showed that the performance of learners could benefit significantly from much larger training sets. Thus, assuming that enough training samples are collected from different persons and from, for example, large vessels—or tissues other than placenta or colon used in this study—the recall of *ARETE* could be improved. We also considered other approaches for improving the performance of *ARETE*. Selinummi (47) presented a system that integrated multiple bright-field images taken at different *z*-levels via relative standard deviation to obtain a higher contrast bright-field image for improved segmentation. However, the authors themselves note in the *Discussion* section that they only used images with low contrast all around the cells, and cells without clearly visible cell borders, whereas our erythrocytes are clearly defined cells with strong borders and high contrast around the cells. Also, because mature erythrocytes are relatively small cells (6–8 μm diameter, ∼2–3 μm height), at most three *z*-levels could be combined, which is the minimum necessary number of *z*-levels to actually compute the relative standard deviation, possibly leading to noisy estimates. Also, taking bright-field images at different *z*-levels takes more time during which the sample needs to be illuminated, which increases photo-bleaching in all fluorescent channels, possibly hampering or disrupting image analysis.

Precision for *ARETE* was 0.52, whereas the experts achieved 0.63. Figure 3d illustrates the cut-out erythrocytes. Obviously, there are pixels next to the found erythrocytes that are FPs. On the contrary, it can also be seen that the erythrocytes are fully captured by the circles, therefore their autofluorescence will not interfere with subsequent target protein quantification.

The F1 score is derived from the precision and recall/sensitivity, therefore the difference (Experts 0.76 vs *ARETE* 0.55) can be explained as in the case of precision and recall. In contrast, the median specificity of *ARETE* was 0.85, which is only about 10% smaller compared with the maximal achievable performance set by the human experts (0.92).

Finally, we also calculated Cohen's κ coefficient, a value that measures the agreement between two raters. Statistical significance for kappa is rarely reported; instead several guidelines have been introduced to define the magnitudes of κ that reflect adequate agreement. When classified according to the scale introduced by Landis and Koch (35), with a Cohen's κ coefficient = 0.41, *ARETE* is only one class below the human performance (moderate vs substantial). When classified according to the scale of Fleiss (36), both the agreement of *ARETE* with experts and the inter-rater agreement were found to be "fair to good." Therefore, we conclude that overall, *ARETE* currently approximates the performance of human experts.

The major benefit of *ARETE* is to perform fast and automatic large-scale analysis of tissue sections and enable meaningful statistical analysis. This is important in the context that although humans are capable of accurate analysis of tissue areas of limited sizes, these areas may not be representative for the entire tissue section (48).

To the best of our knowledge, *ARETE* is the first prototype that operates on nonstained tissues. By manipulating acquired microscopic images with erythrocyte masks, it is possible to combine *ARETE* in a workflow with open source and commercially available software such as TissueQuest (TissueGnostics GmbH).

With suitable training samples, the future applications of *ARETE* may include the detection and quantification of healthy erythrocytes in order to study vasculo-/angiogenesis and pathologically altered erythrocytes in metabolic or infectious diseases (49).

Conflict of interest statement

This article is based on the work of a thesis at the Medical University of Vienna (MedUniWien), Vienna, Austria, by Andreas Heindl. Radu Rogojanu is an employee of TissueGnostics GmbH (TG), a company that provides software for the analysis of tissue cytometry data. This research project (BRIDGE project) was mainly funded by FFG (Vienna, Austria) and TG. MedUniWien, Seewald Solutions, and TG collaborated to develop new image segmentation algorithms. The described system *ARETE* was implemented as part of this research project. The company TissueGnostics has exclusive commercial use of *ARETE*. Coauthor Radu Rogojanu is directly employed by TissueGnostics and thus declares a conflict of interest.

References

1. Tarnok A. Slide-based cytometry for cytomics—a minireview. Cytometry A 2006;69A:555–562.
2. Carpenter AE, Jones TR, Lamprecht MR, Clarke C, Kang IH, Friman O, Guertin DA, Chang JH, Lindquist RA, Moffat J and others. CellProfiler: Image analysis software for identifying and quantifying cell phenotypes. Genome Biol 2006;7:R100.
3. Lamprecht MR, Sabatini DM, Carpenter AE. CellProfiler: Free, versatile software for automated biological image analysis. Biotechniques 2007;42:71–75.
4. Hamilton N. Quantification and its applications in fluorescent microscopy imaging. Traffic 2009;10:951–961.
5. Huang D, Casale GP, Tian J, Lele SM, Pisarev VM, Simpson MA, Hemstreet GP, 3rd. Udp-glucose dehydrogenase as a novel field-specific candidate biomarker of prostate cancer. Int J Cancer 2010;126:315–327.
6. Bodo J, Durkin L, Hsi ED. Quantitative in situ detection of phosphoproteins in fixed tissues using quantum dot technology. J Histochem Cytochem 2009;57:701–708.
7. Waters JC. Accuracy and precision in quantitative fluorescence microscopy. J Cell Biol 2009;185:1135–1148.
8. Robertson D, Isacke CM. Multiple immunofluorescence labeling of formalin-fixed paraffin-embedded tissue. Methods Mol Biol 2011;724:69–77.
9. Remmele W, Stegner HE. [Recommendation for uniform definition of an immunoreactive score (IRS) for immunohistochemical estrogen receptor detection (ER-ICA) in breast cancer tissue]. Pathologe 1987;8:138–140.
10. Conway C, Dobson L, O'Grady A, Kay E, Costello S, O'Shea D. Virtual microscopy as an enabler of automated/quantitative assessment of protein expression in TMAs. Histochem Cell Biol 2008;130:447–463.
11. Del Castillo P, Llorente AR, Stockert JC. Influence of fixation, exciting light and section thickness on the primary fluorescence of samples for microfluorometric analysis. Basic Appl Histochem 1989;33:251–257.
12. Khandelwal S, Saxena RK. Age-dependent increase in green autofluorescence of blood erythrocytes. J Biosci 2007;32:1139–1145.

13. Vigneshwaran N, Bijukumar G, Karmakar N, Anand S, Misra A. Autofluorescence characterization of advanced glycation end products of hemoglobin. Spectrochim Acta A Mol Biomol Spectrosc 2005;61:163–170.
14. Negre-Salvayre A, Salvayre R, Auge N, Pamplona R, Portero-Otin M. Hyperglycemia and glycation in diabetic complications. Antioxid Redox Signal 2009;11:3071–3109.
15. Vicente Miranda H, Outeiro TF. The sour side of neurodegenerative disorders: the effects of protein glycation. J Pathol 2010;221:13–25.
16. Chekir C, Nakatsuka M, Noguchi S, Konishi H, Kamada Y, Sasaki A, Hao L, Hiramatsu Y. Accumulation of advanced glycation end products in women with preeclampsia: possible involvement of placental oxidative and nitrative stress. Placenta 2006;27:225–233.
17. Yu Y, Hanssen K, Kalyanaraman V, Chirindel A, Jenkins A, Nankervis A, Torjesen P, Scholz H, Henriksen T, Lorentzen B and others. Reduced soluble receptor for advanced glycation end-products (sRAGE) scavenger capacity precedes pre-eclampsia in Type 1 diabetes. BJOG 2012;119:1512–1520.
18. Baschong W, Suetterlin R, Laeng RH. Control of autofluorescence of archival formaldehyde-fixed, paraffin-embedded tissue in confocal laser scanning microscopy (CLSM). J Histochem Cytochem 2001;49:1565–1572.
19. Mosiman VL, Patterson BK, Canterero L, Goolsby CL. Reducing cellular autofluorescence in flow cytometry: an in situ method. Cytometry 1997;30:151–156.
20. Schnell SA, Staines WA, Wessendorf MW. Reduction of lipofuscin-like autofluorescence in fluorescently labeled tissue. J Histochem Cytochem 1999;47:719–730.
21. Billinton N, Knight AW. Seeing the wood through the trees: a review of techniques for distinguishing green fluorescent protein from endogenous autofluorescence. Anal Biochem 2001;291:175–197.
22. Viegas MS, Martins TC, Seco F, do Carmo A. An improved and cost-effective methodology for the reduction of autofluorescence in direct immunofluorescence studies on formalin-fixed paraffin-embedded tissues. Eur J Histochem 2007;51:59–66.
23. Diaz G, Gonzalez FA, Romero E. A semi-automatic method for quantification and classification of erythrocytes infected with malaria parasites in microscopic images. J Biomed Inform 2009;42:296–307.
24. Albertini MC, Teodori L, Piatti E, Piacentini MP, Accorsi A, Rocchi MB. Automated analysis of morphometric parameters for accurate definition of erythrocyte cell shape. Cytometry A 2003;52A:12–18.
25. Cohen J. A Coefficient of Agreement for Nominal Scales. Educational and Psychological Measurement 1960;20:37–46.
26. Fleiss J, Cohen J. The equivalence of weighted kappa and the intraclass correlation coefficient as measures of reliability. Educ Psychol Meas 1973;33:6.
27. Ramasamy R, Yan SF, Schmidt AM. Receptor for AGE (RAGE): Signaling mechanisms in the pathogenesis of diabetes and its complications. Ann N Y Acad Sci 2011;1243:88–102.
28. Heindl A, Dekan S, Ellinger I, Seewald AK. Towards a versatile automated cell-detection system for science and diagnostics. Conf Proc IEEE Eng Med Biol Soc 2010;2010:3045–3048.
29. Oliver EA, Buhimschi CS, Dulay AT, Baumbusch MA, Abdel-Razeq SS, Lee SY, Zhao G, Jing S, Pettker CM, Buhimschi IA. Activation of the receptor for advanced glycation end products system in women with severe preeclampsia. J Clin Endocrinol Metab 2011;96:689–698.
30. Demir R, Akkoyunlu G. The fine and three-dimensional observations on the basal plate surface and anchoring villi in mature human placenta. Scanning 1998;20: 253–254.
31. Viola P, Jones M. Rapid object detection using a boosted cascade of simple features. 2001. p I-511–I-518 vol.1.
32. Freund Y, Schapire R. Experiments with a New Boosting Algorithm. In International Conference on Machine Learning; 1996. p 148–156.
33. Lienhart R, Maydt J. An extended set of Haar-like features for rapid object detection. 2002. p I-900–I-903 vol.1.
34. Blair DC. Chapter 7: Evaluation. In: Van Rijsbergen CJ, editor. Information Retrieval, 2nd ed. London: Butterworths; 1979. 208 pp.
35. Landis JR, Koch GG. The measurement of observer agreement for categorical data. Biometrics 1977;33:159–174.
36. Fleiss J, Levin B, Paik M. Chapter 18: The Measurement of Interrater Agreement. In: Shewart WA, Samuel S. Wilks SS, editors. Statistical Methods for Rates and Proportions, 3rd Ed. Wiley-Interscience; 2003; ISBN 9780471526292.
37. Wilson SB, Emerson R. Spike detection: A review and comparison of algorithms. Clin Neurophysiol 2002;113:1873–1881.
38. Anjomshoaa A, Lin YH, Black MA, McCall JL, Humar B, Song S, Fukuzawa R, Yoon HS, Holzmann B, Friederichs J and others. Reduced expression of a gene proliferation signature is associated with enhanced malignancy in colon cancer. Br J Cancer 2008;99:966–973.
39. Baschong W, Duerrenberger M, Mandinova A, Suetterlin R. Three-dimensional visualization of cytoskeleton by confocal laser scanning microscopy. Methods Enzymol 1999;307:173–189.
40. Geismann P, Schneider G. A two-staged approach to vision-based pedestrian recognition using Haar and HOG features. Proc. of the IEEE Intelligent Vehicles Symposium, Eindhoven, The Netherlands, 4–6 June 2008. p 554–559.
41. Qing C, Georganas ND, Petriu EM. Real-time Vision-based Hand Gesture Recognition Using Haar-like Features. Proc. of the Instrumentation and Measurement Technology Conference (IMTC), Warsaw, Poland, 1–3 May 2007. p 1–6.
42. Jiang S, Zhou X, Kirchhausen T, Wong ST. Detection of molecular particles in live cells via machine learning. Cytometry A 2007;71:563–575.
43. Zaritsky A, Natan S, Horev J, Hecht I, Wolf L, Ben-Jacob E, Tsarfaty I. Cell motility dynamics: A novel segmentation algorithm to quantify multi-cellular bright field microscopy images. PLoS One 2011;6:e27593.
44. Nielsen B, Albregtsen F, Danielsen HE. Automatic segmentation of cell nuclei in Feulgen-stained histological sections of prostate cancer and quantitative evaluation of segmentation results. Cytometry A 2012;81A:588–601.
45. Bessis M. Red cell shapes. An illustrated classification and its rationale. Nouv Rev Fr Hematol 1972;12:721–745.
46. Banko M, Brill E. Scaling to very very large corpora for natural language disambiguation. Proceedings of the 39th Annual Meeting on Association for Computational Linguistics. Toulouse, France: Association for Computational Linguistics; 2001. p 26–33.
47. Selinummi J, Ruusuvuori P, Podolsky I, Ozinsky A, Gold E, Yli-Harja O, Aderem A, Shmulevich I. Bright field microscopy as an alternative to whole cell fluorescence in automated analysis of macrophage images. PLoS One 2009;4:e7497.
48. Camp RL, Charette LA, Rimm DL. Validation of tissue microarray technology in breast carcinoma. Lab Invest 2000;80:1943–1949.
49. Muehlenbachs A, Fried M, McGready R, Harrington WE, Mutabingwa TK, Nosten F, Duffy PE. A novel histological grading scheme for placental malaria applied in areas of high and low malaria transmission. J Infect Dis 2010;202:1608–1616.